CrystEngComm

Accepted Manuscript

ROYAL SOCIETY OF CHEMISTRY

www.rsc.org/crystengcomm

One-pot synthesis of Ag@Cu yolk-shell nanostructures and their application as nonenzymatic glucose biosensor

Shuling Xu[a], Haibo Li[a], Lei Wang[a], Qiaoli Yue[a], Sun Sixiu[b] and Jifeng Liu[a]

[a] *Department of Chemistry, liaocheng University, liaocheng, Shandong 252059, PR China*

[b] *Department of Chemistry, Shandong University, Jinan, Shandong 250100, PR China*

E-mail: liujifeng111@gmail.com

In this report, Ag@Cu yolk-shell nanostructures have been synthesized through a facile one-pot hydrothermal method. The synthesis is based on the use of *N*, *N*-Dimethylformamide (DMF) as both reducing agent and solvent, in the presence of the polymer-poly(vinylpyrrolidone) (PVP). The structure and composition of the yolk-shell nanostructures were characterized by X-ray diffraction (XRD), scanning electron microscopy (SEM), transmission electron microscopy (TEM), and energy dispersive spectrometer (EDS). To study the formation process of Ag@Cu yolk-shell nanostructures, the samples obtained at various stages of the growth process were studied by TEM and XRD, and a rational growth mechanism of the Ag@Cu yolk-shell nanostructures is proposed. The as-prepared Ag@Cu yolk-shell nanostructures were used to construct nonenzymatic glucose sensors. The detecting results show that the designed sensors have well-defined, stable and fast amperometric responses to glucose.

1. Introduction

In recent years, bimetallic nanoparticles have received intensive attention because of their novel optical, electronic, magnetic, and catalytic properties, which differ from those of their respective constituent metals [1-5]. It has been noted that the shape, composition, and architecture are being recognized as important control parameters in the tailoring of new bimetallic nanostructures [6-7]. Very recently, a number of bimetallic core-shell nanoparticles with well-defined geometries have been investigated through conformal epitaxial growth of the second metal over the pre-synthesized seed nanoparticles [8-12]. In particular, a new class of core-shell structures with a distinctive core-void-shell configuration, which are called yolk-shell, or cage-bell structures, has attracted much attention in a diverse range of applications [13-15]. Compared with core-shell composites, they possess higher surface area, larger void space and lower density, which lead to wide applications in drug delivery, lithium-ion batteries and catalysis [16]. Therefore, considerable attentions have been paid to preparation of yolk-shell composites [17-19].

Bimetallic nanostructures are considered to be a kind of excellent candidate for electrocatalysis, sensing due to their potential in electrode modification by enhancing the electrode conductivity, facilitating the electron transfer, and improving the analytical sensitivity and selectivity [20-24]. Especially, bimetallic nanostructures exhibited the superior electrocatalytic activity and selectivity toward the oxidation of glucose [25]. Among these materials, the Cu-based bimetallic nanoparticles as an important class of nanostructure have been attracted increasingly attention owning to the high electrical conductivity and low cost of Cu. There have been several reports regarding non-enzymatic glucose sensors based on Cu-based bimetallic nanoparticles [26-29]. The performances of those sensors were improved greatly. In such case, the foreigner element may enhance the catalytic activity of Cu via electronic effect of ligand or bifunctional effect [30].

Herein, taking the enhanced performance of glucose sensors into account, we seek the bimetallic nanostructures which contain Cu to study their sensor activity. Considering the excellent electronic transport and catalytic properties of Ag, it is chosen as the second metal. However, because of large lattice mismatch (e.g., 13% for Cu and Ag) and complicated reaction environment, synthesis of such hetero-structural configuration in solution phase is a challenge issue in current chemistry and material science [31]. In this work, we describe a one-step, simple, and effective method to synthesize Ag@Cu yolk-shell nanostructures with a high yield. The electrochemical performance of the modified electrode was investigated by cyclic voltammetry and chronoamperometry. In addition, we further demonstrated that such Ag@Cu yolk-shell nanostructures could serve as a promising probe material for enhancing non-enzymatic glucose sensing.

2. Experimental Section

2.1 Chemicals and Reagents

All of the chemicals were analytical reagent grade and used as purchased without further purification. Silver nitrate ($AgNO_3$), $Cu(NO_3)_2\cdot 3H_2O$ and *N,N*-dimethylformamide (DMF) were purchased from Sinopharm Chemical Reagent Co., Ltd. (Shanghai, China). All chemical reagents were of analytical grade and used without further purification. Polyvinylpyrrolidone (PVP) with Mw of 58 000 was purchased from Aladdin Co. (Shanghai). Water used in this work was prepared from a Milli-Q water purification system (≥18 MΩ cm).

2.2 Synthesis of Ag@Cu yolk–shell nanostructures

All of the chemical reagents in this experiment were analytical grade, and used without further purification. In a typical synthesis, 0.1 mL of 0.5 M $AgNO_3$ was added into 20 mL DMF with magnetic stirring. And then 0.05 g $Cu(NO_3)_2·3H_2O$ and 0.01 g PVP were dissolved into the above solution, respectively. After being vigorously stirred for 10 min, the mixture was put into a Teflon-lined autoclave of 25-mL capacity and maintained at 160 □ for 24 h, then cooled to room temperature naturally. The products were collected, and washed thoroughly with deionized water and absolute ethanol. Finally they were dried in a vacuum oven before further characterization.

2.3 Electrochemical Measurements

Bare glassy carbon electrode (GCE, dia. 3 mm) was polished with alumina slurries, and then successively sonicated in acetone, ethanol, and water followed by drying at room temperature. An appropriate volume of Ag@Cu yolk-shell nanostructures /ethanol suspension (5 mg/mL) was dropped on the surface of GCE. After drying in air, 2μL of Nafion (0.1 wt%) was then cast on the layer of Ag@Cu yolk-shell nanostructures for the purpose of entrapment. The as-prepared electrode is denoted as Nafion/ACN/GCE. The electrochemical experiments were carried out with a CHI 760B electrochemical workstation (Shanghai Chenhua Co., China) with a conventional three-electrode cell. The modified or unmodified GCE was used as the working electrode. The Pt wire and Ag/AgCl (3.0 M KCl) electrode were used as the counter and reference electrodes, respectively. All potentials in this work were given versus the Ag/AgCl electrode.

2.4 Physical characterizations

The samples were characterized by XRD on a German Bruker D8 X-ray diffractometer with Ni filtered Cu Kα radiation (λ=1.5418 Å). The morphology was characterized with a JEM-100CX2 transmission electron microscope (TEM) and a Hitachi S-4800 scanning electron microscope (SEM), and the composition was characterized by an energy dispersive spectrometer (EDS) attached to the SEM and FE TEM, FEI TECNAI G2. A high-resolution TEM (HRTEM) image was characterized using a JEOL 2100 transmission electron microscope. The UV-vis absorption spectra were recorded with a Hitachi U-4100 spectrophotometer.

3. Results and Discussion

3.1 Characterization of Ag@Cu yolk-shell nanostructures

The phase and purity of the as-obtained products are examined by XRD. Fig. 1 shows a typical XRD pattern of the products. The four peaks located at 38.0, 44.1, 64.3, and 77.5 in the pattern can be indexed to the diffraction from the (111), (200), (220), and (311) planes of face-centered cubic Ag (JCPDS file NO. 04-0783). The three peaks at 43.4, 50.5, and 74.1 are assigned to be (111), (200) and (220) diffraction planes of the face-centered cubic structure of metallic Cu (JCPDS file NO. 04-0836). This indicates that the prepared products via this method are composed of Ag-Cu bimetallic nanostructures.

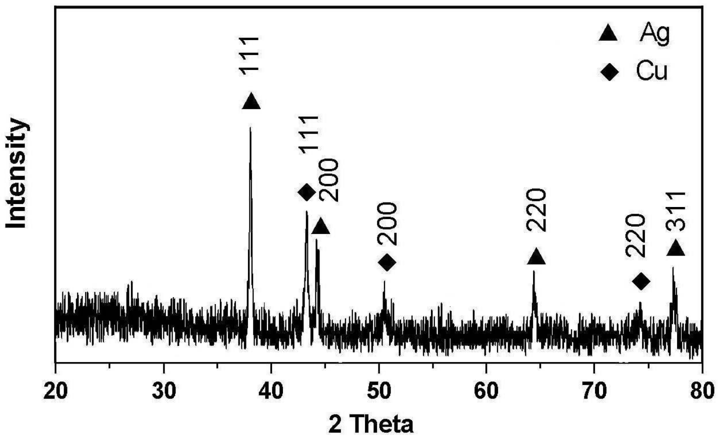

Fig. 1 XRD pattern of the Ag@Cu yolk-shell nanostructure.

TEM and SEM investigations are employed to obtain information about the morphology and the structure of the bimetallic nanostructures. The TEM image (Fig. 2a) clearly shows that the resulting product consists of quasi-spheres with size of about 200-400nm and some nanorods in the length of 300-400nm. The atrous solid core of the sample contrasts strongly with the lighter region corresponding to the void region between the yolk and the shell, which provides direct evidence that the as-prepared nanostructures have a yolk-shell structure. The SEM image of the bimetallic nanostructures is shown in Fig. 2b. It is interesting that an individual nanoparticle displays the broken site and exposes the yolk-shell structure, as shown at the arrow, the boundary between the yolk and the shell can be clearly observed, which is consistent with the TEM analysis.

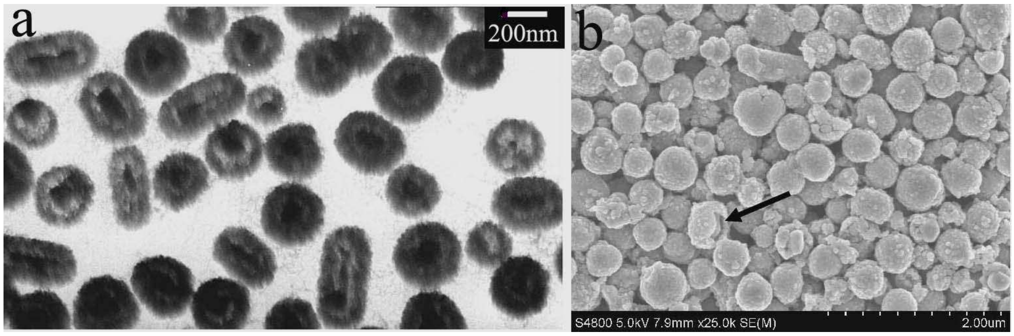

Fig. 2 (a) TEM (b) SEM images of the Ag@Cu yolk-shell nanostructure.

To examine the detailed structure of the yolk-shell nanostructures, the high-resolution SEM images were performed. The typical SEM images of the crashed shell and the partially broken yolk-shell nanostructures are shown in Fig. 3a and 3b, respectively. It can be clearly observed that the surfaces of the shell are not smooth, suggesting that the shell are made from an aggregation of smaller particles. Energy-dispersive spectroscopy (EDS) is used to probe the chemical compositions of the as-prepared yolk-shell nanostructures. Fig. 3c and 3d show the comparison of EDS spectra acquired by positioning the electron probe through only the shell (Fig. 3a) and through the partially broken yolk-shell nanostructures (Fig. 3b), respectively. It is apparent that the shell nanostructures is dominated by Cu (the Al signal is from the aluminum foil), no peak from Ag can be detected in the EDS spectrum, indicating the shell of the nanostructures is Cu. The partially broken yolk-shell nanostructure is rich in Ag and Cu, suggesting that the yolk of the nanostructures is Ag. The EDX line scanning spectroscopy across the representative Ag@Cu yolk-shell nanostructure is shown in Fig. 3e. A single Ag nanoparticle (green signal) was located in the yolk region of the nanoparticle, while several distinct Cu nanoparticles (red signal) were decorated in the outer regions. The EDS data shows that the ratio of Ag atom to Cu atom is 32:68 for the product. The results indicated that the as-prepared nanoparticles have Ag@Cu yolk-shell structure. The HRTEM image (Fig. S1) reveals a lattice fringe of 0.21 nm of the overlayer that corresponds to the lattice fringe of Cu (111) crystal plane.

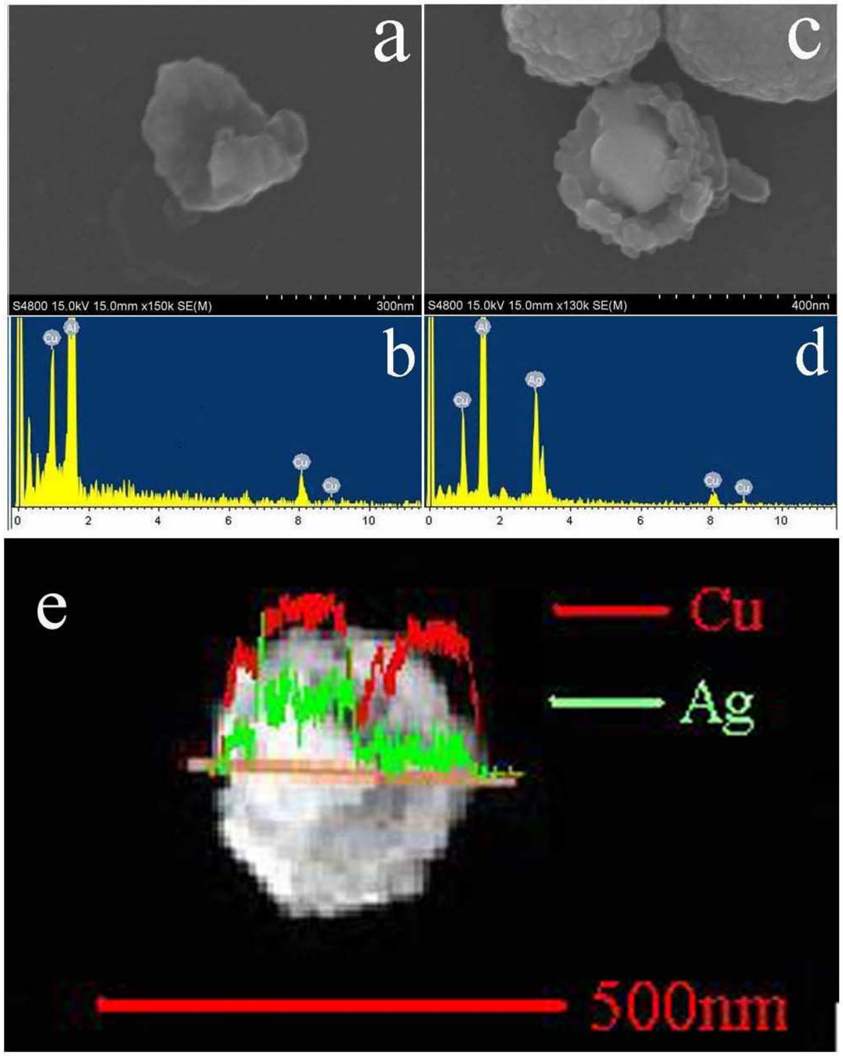

Fig. 3 (a) SEM image of an individual broken shell; (b) SEM images of an individual partially broken Ag@Cu yolk-shell nanostructure; Comparison of the EDS spectra acquired from (c) the shell and (d) the yolk of the Ag@Cu yolk-shell nanostructure. (e) EDX line-scanning profile across the representative Ag@Cu yolk-shell nanostructure.

To investigate the evolution process of the Ag@Cu yolk-shell nanostructure, time-dependent experiments are carried out and the samples collected from the reaction solution at various stages are characterized by XRD patterns and TEM images. Fig. 4a provides XRD pattern of the samples formed after 4h. As can be seen, apart from all of the obvious diffraction peaks at 38.0, 44.1, 64.3, and 77.5 corresponding to face-centered cubic Ag, the peaks at 36.5 and 61.4 are assigned to (111) and (220) planes of the cubic phase Cu_2O (JCPDS file No.05-0667), indicating that there also possibly coexists of Cu_2O in the products. When the reaction proceeded for 12 h, the faint peaks at 74.1 can be indexed to (220) of plane face-centered cubic Cu, which means a trace amount of Cu coexists with Ag and Cu_2O particles in the samples at this stage (as shown in Fig. 4b). Fig. 4c gives the XRD pattern of the resultant products prepared after 18h, from which we can see that the intensity of the Cu peaks increases. With the reaction time further increases to 24 h, from the XRD patter of Fig. 1, the peak of Cu_2O disappeared and the samples consisted of Ag and Cu.

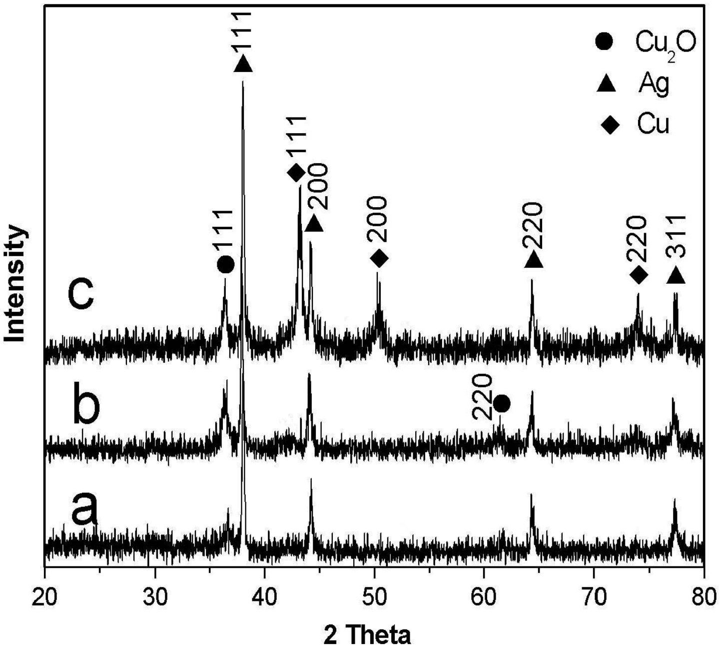

Fig. 4 XRD pattern of nanoparticles obtained at 160℃ at different reaction times: (a) 4 h; (b) 12 h; (c) 18h.

UV-vis spectra of nanostructures strongly depended on the composition and surface plasmon resonance (SPR) property of nanostructures. UV-vis spectra of the nanoparticles obtained at different time are shown in Fig. S2. From it, we can see that the samples obtained at 4 h shows a broad peak centered at 492 nm (curve a), which is attributed to Ag nanocrystals [32]. No peaks concerning Cu_2O or Cu appeared. When the reaction time is prolonged to 10 h, the peak at 492 nm shifted to 499 nm, as shown in curve b, which has contributed to the increase of the silver nanoparticle size. At the same time, the corresponding absorption peak of Cu_2O appears at around 609 nm is observed as shown in curve b [33]. When the reaction time was prolonged to 18 h, along with the transformation of Cu_2O to Cu, the peak at 499 nm is still present and the peak at 609 nm shifted to 605 nm and the intensity of the peak increases, as shown in curve c. The UV-visible spectra of the prepared nanostructure obtained at 24 h, two peaks are observed at about 499 nm and 602 nm as shown in curve d, which are attributed to the SPR of Ag and Cu nanoparticle, respectively [34].

Corresponding to the above phase evolution, the time dependent crystal morphology of the samples is reported. Fig. 5a-c show typical TEM images of the products obtained after 4, 12 and 18 h solvothermal treatment, respectively. It is obvious that a mixture of nanoparticles with different irregular morphologies were formed at a reaction time of 4h (Fig. 5a). When the reaction time was prolonged to 12 h, quasi-spheres and rods began to appear but the apertures between core and shell were unconspicuous (Fig. 5b). After the reaction proceeded for 18 h, the core-shell structure takes place and the brightness contrast between the core and the shell is observed, indication their yolk-shell structure (Fig. 5c).

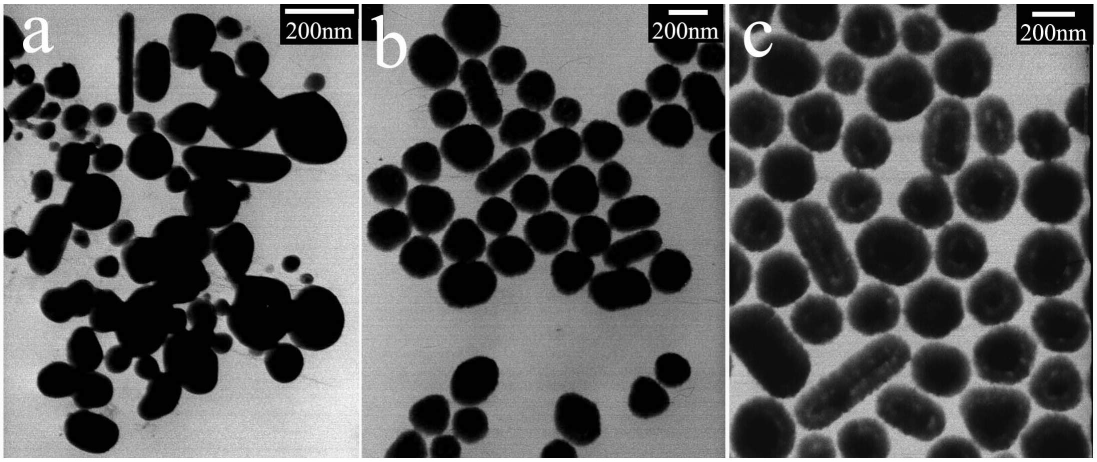

Fig. 5 TEM images of nanoparticles obtained at 160℃ at different reaction times: (a) 4 h; (b) 12 h; (c) 18h.

We also investigated the role of PVP in the formation of Ag@Cu yolk-shell nanostructures. Firstly, we prepared Ag@Cu yolk-shell nanostructures without PVP under the typical conditions described in the experimental section. TEM image of the products is shown in Fig. S3a, one can see that, the products are mainly spherical Ag@Cu yolk-shell nanostructures，but the void spaces between the Ag@Cu nanostructure are inhomogeneous, the void spaces between the Ag@Cu nanostructures are inhomogeneous, some places do not even see the existence of the gap. It is noted that PVP has a structure of a polyvinyl skeleton with polar groups. The donated lone pairs of both nitrogen and oxygen atoms in the polar groups of one PVP unit may occupy orbitals of the metal ion to form a complex. The as-formed complex leads to a homogeneous precursor for the synthesis of Ag@Cu yolk-shell nanostructures. When the amount of PVP reaches 0.02g, large rod-like Ag@Cu yolk-shell nanostructures are formed. As we know, the formations of the rod-like nanostructure first need the anisotropy during the growing process for the nanoparticles [35]. The selective interaction of the PVP molecules on the facets of the first-formed nanoparticles is crucial to the anisotropic growth of nanostructures. Hence, in our method, the high PVP concentration was suppress the preferential growth of the Ag@Cu yolk-shell nanostructures. These results clearly suggest that PVP is essential for the formation of homogeneous Ag@Cu yolk-shell nanostructures.

Formation process of the Ag@Cu yolk-shell nanoparticles

DMF has been demonstrated to be an effective reducing agent for the preparation of metal nanoparticles with tunable shape and size under suitable condition, it can reduce Ag^+ to Ag nanoparticles even at room temperature, and the reaction rate is markedly increased at higher temperatures [36-37]. The standard redox potential of Ag^+/Ag pair (+0.78 eV) is higher than that of Cu^{2+}/Cu pair (+0.34 eV). Therefore, the reduction of Ag^+ occurs more rapidly than Cu^{2+} when Ag^+ and Cu^{2+} present in the DMF at the same time. At the early reaction stage, Ag^+ are reduced to Ag^0 first (equation 1), which act as the core of the yolk-shell structure. On the basis of the above XRD results in Fig. 4, it is believed that the forming of Cu via reducing of Cu^{2+} with DMF can be divided into two stages, first to Cu_2O (equation 2a) and then to Cu^0 (equation 2b).

$$Ag^+ + e \rightarrow Ag^0 \quad (1)$$

$$Cu^{2+} + e \rightarrow Cu^+ \quad (2a)$$

$$Cu^+ + e \rightarrow Cu^0 \quad (2b)$$

According the above results, the formation mechanism of the Ag@Cu yolk-shell nanostructures is proposed. Galvanic replacement offers a facile and versatile route to a variety of nanostructures characterized by tightly controlled sizes and shapes, hollow interiors, porous walls, and tunable elemental compositions [38]. Considering that the Ag has a much higher reduction potential than that of Cu, there might be a galvanic replacement between Ag^+ and Cu. However, in our reaction system, Ag and Cu are in the form of Ag^+ and Cu^{2+} in DMF, Ag^+ are reduced to Ag^0 first, therefore, we could establish that the galvanic replacement is inappropriate for the evolution process of the Ag@Cu yolk-shell nanostructure.

In the formation process of the Ag@Cu yolk-shell nanostructures, the obtained Ag nanoparticles are acting as nucleic centers for growth of the yolk-shell nanostructures. As the reaction progresses, Cu^{2+} ions are reducing to Cu_2O surrounding the Ag nanoparticles and $Ag@Cu_2O$

nanoparticles are formed. With the reaction time increasing, DMF reacts with the Cu_2O on the surface of the Ag@Cu_2O nanoparticles and the Cu nanoparticles are formed on the outside surfaces of the Cu_2O nanoparticles shell. The formation of Cu nanoparticles layer does not prevent further chemical reduction reaction between the Cu_2O nanoparticles and DMF. Under high temperature, the diffusion rate of copper ions in Cu_2O nanoparticles is faster than that of oxygen ions [39], which is named as the Kirkendall effect, this leads to that the continuous reduction reaction is limited on the outer surface and could not be extended to the interior space. Therefore, accompanied by the outward diffusion and reduction of copper ions, the void spaces between the core and shell are developed. A schematic illustration of the proposed formation mechanism of the Ag@Cu yolk-shell nanostructures is shown in Fig. 6. It should be pointed out that, the lattice constants between Ag and Cu are quite different，a large lattice mismatch may be helpful for the formation of yolk-shell in the synthesis. At the same time, a higher reaction temperature is required to overcome the relatively higher energy barrier to surface diffusion [40]. The reaction was carried out at 160 ℃，at this high temperature, Cu atom diffusion rate will be greatly increased. This increased diffusion rate of Cu atom will overcome the difference in lattice constant and promote the overgrowth of a conformal Cu layer. Finally, until all copper ions are completely transformed to Cu nanoparticles by reacting with DMF, and the Ag@Cu yolk-shell nanostructures are formed.

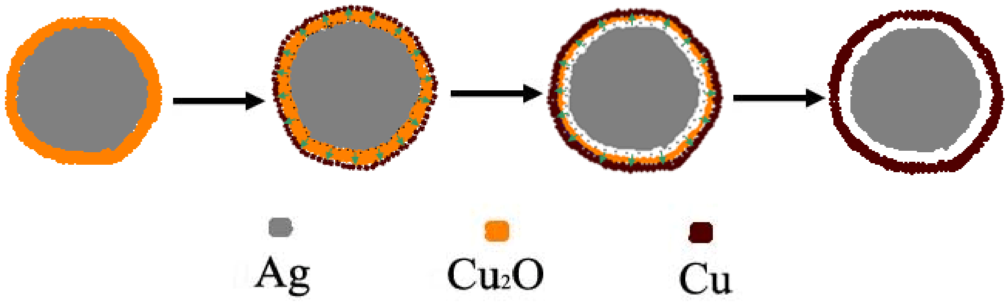

Fig. 6. Schematic illustration of growth mechanism of the Ag@Cu yolk-shell nanostructures.

Non-enzymatic amperometric sensing of glucose

The as-prepared Ag@Cu yolk-shell nanoparticles are employed as glucose sensing anode materials.

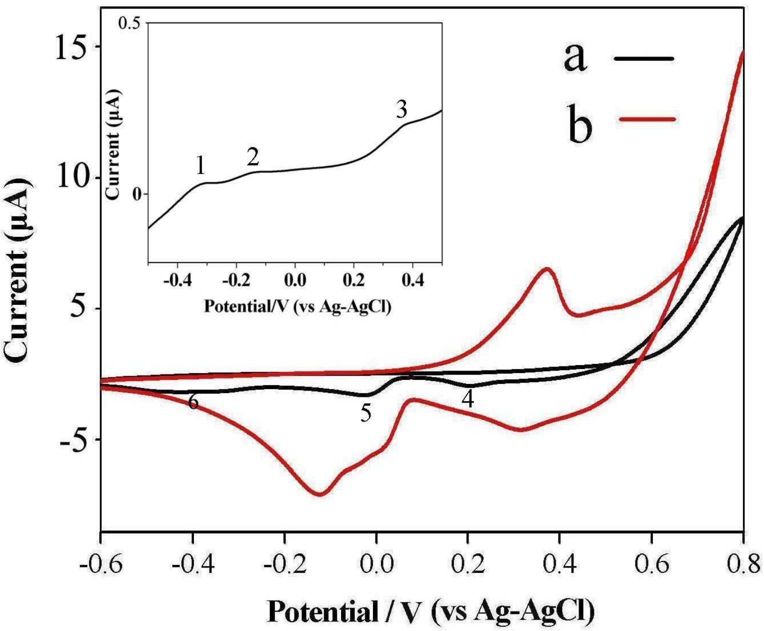

Figure 7. CVs of the ACN/Nafion/GCE in the absence (a) and in the presence of 1 mM (b) glucose in 0.1 M NaOH. Scan rate: 50 mV/s.

The electrocatalytic activity of the ACN/Nafion/GCE towards the oxidation of glucose in an alkaline medium was investigated. Fig. 7 presents the cyclic voltammograms (CVs) of the ACN/Nafion/GCE in the absence (a) and presence (b) of 1 mM glucose in 0.1 M NaOH. The inset graph in Fig. 7 is an augmentation of the curve (a). Peak 1 is due to the transition of Cu(0)/Cu(I). Peak 2 involves the transition of Cu(0)/Cu(I I) as well as Cu(I)/ Cu(II). Although, no apparent wave emerging, it is generally believed that the oxidation of Cu(II) to Cu(III) is initialized at about 0.6 V in high concentration of NaOH solution. Peaks 4, 5, and 6 in the cathodic scan can be attributed to the transition of Cu(III)/Cu(II), Cu(II)/Cu(I), and Cu(I)/Cu(0), respectively [41]. In the presence of 1 mM glucose (b), a very large oxidation current was observed at 0.35 V during the cathodic scan, representing pronounced glucose oxidation.

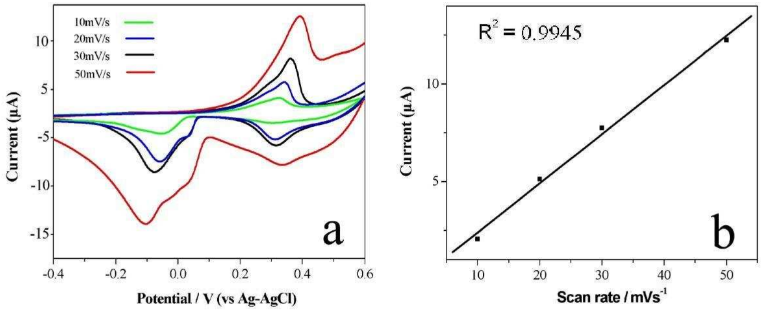

Fig. 8. (a) CV curves of 2 mM glucose in a 0.1 M NaOH solution on the ACN/Nafion/GCE electrode at different scan rates. (b) The calibration plot of oxidation peak current vs. scan rate.

Fig. 8a shows the effect of scan rates on the electro-oxidation of glucose at the ACN/Nafion/GCE electrode in the alkaline solution. The calibration plot (Fig. 8b) exhibits a good linear relationship between the oxidation peak current density and scan rate, indicating that the electrode reaction is a surface-controlled process.

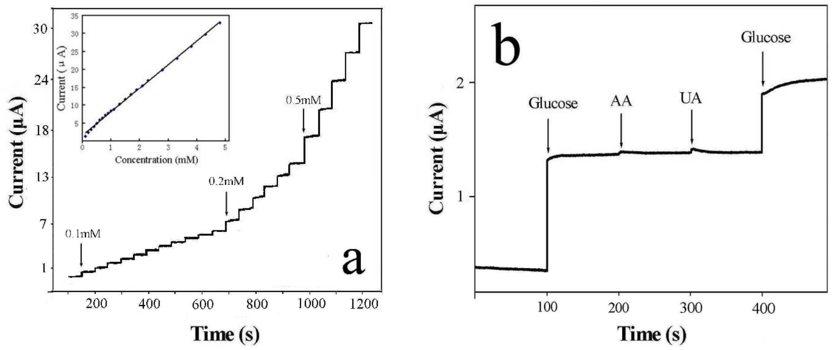

Figure 9. (a) Typical amperometric response of ACN/Nafion/GCE to successive injection of glucose into 0.1 M NaOH with stirring, the working potential was 0.35 V. Inset shows calibration curve and linear plot of response current vs glucose concentration. (b) Amperometric response for successive injection of 0.2 mM glucose and interfering species (0.2 mM UA and 0.2 mM AA) into 0.1 M NaOH with stirring, the working potential was 0.35 V.

The amperometric response of the ACN/Nafion/GCE upon successive addition of glucose to 0.1 M NaOH at an applied potential of 0.35 V is shown in Fig. 9a. It can be observed that the ACN/Nafion/GCE electrode responds quickly and reaches a steady-state current within 2s, indicating ACN/Nafion/GCE sensor exhibits extremely rapid and sensitive response characteristics toward glucose. As shown in bottom inset of Fig. 9a, the current response i (μA) vs. glucose concentration (mM) in the range of 0.1-4.8mM exhibits a good linearity with a correlation coefficient R^2=0.9932. The detection limits is 3 μ M at a signal-to-noise ratio of 3. The performance of our proposed glucose sensor is compared with some reported Cu and Ag materials based non-enzymatic glucose sensors and the results are summarized in Table 1.The sensitivity and the detection limit of our ACN/Nafion/GCE were inferior to same of non-enzymatic electrodes mentioned above, however, ACN/Nafion/GCE has the superior response speed.

Table 1

Comparison of the present CuS NTs based glucose sensor with other materials based nonenzymatic glucose sensors.

Electrode material	Response time	Linear range	Detection limit	Reference
Ag nanoparticles	——	0.5 mM to 75 mM	0.5μM	42
GOD-CS/AgNWs	10 s	10μM to 0.8 mM	2.83μM	43
Cu-Ag_2O NWS	5 s	0.2 mM to 3.2 mM	0.01 mM	44
Cu flowers	——	2μM to 75μM	1μM	45
Au@Pd-ILs–Au@Pd	——	5 nM to 0.5μM	1.0nM	46
Ni–Cu-oxide	4s	0.1μM to 1200μM	0.1μM	47
ACN/Nafion/GCE	2s	0.1mM to 4.8mM	3μM	This work

One of the most important analytical factors for a glucose sensor is the selectivity to target analyte because easily oxidative species such as ascorbic acid (AA) and uric acid (UA) coexist with glucose in human blood. Thus, we conducted the interference test by measuring currents changes caused by addition of AA and UA during glucose sensing. Because the normal physiological level of glucose is substantially higher than the interfering agents, the anti-interference effect of the modified as-prepared ACN/Nafion/GCE was tested by addition of 0.2mM glucose at 0.35 V, followed by the additions of 0.2mM AA, 0.2mM UA and 0.1 mM glucose gradually in a 0.1 M NaOH solution, as shown in Figure 9b. It is clearly observed that an obvious glucose response was obtained, while insignificant current responses were seen for interfering species compared to glucose addition. The observations demonstrate that Ag@Cu yolk-shell nanoparticles have a good specificity for glucose detection in the presence of a relatively low concentration of coexisting interfering agents.

Conclusions

In summary, we have synthesized Ag@Cu yolk-shell nanostructures by a facile, one-pot hydrothermal method. The growth process of Ag@Cu yolk-shell nanostructures was investigated, revealing that the yolk–shell structure is formed by Kirkendall effect. Such Ag@Cu yolk-shell nanostructures serving as a promising electrode material for nonenzymatic glucose sensor shows a linear response in the concentration ranging from 0.1-4.8 mM at 0.35 V and good selectivity against common interfering species. This approach provided a simple method to develop a new kind of electrochemical sensor. We anticipate that upon further development, these Ag@Cu yolk-shell nanostructures electrodes will perform exceptionally in glucose sensing applications.

Acknowledgements

This work was supported by the National Natural Science Foundation of China (Grant No. 21105041), and Natural Science Foundation (ZR2010BZ004, ZR2012BM007, JQ201106) of Shandong Province.

References

(1) M. A. Mahmoud and M. A. El-Sayed, *Langmuir*, 2012, **28**, 4051-4059.

(2) B. Lim, H. Kobayashi, T. Yu, J. Wang, M. J. Kim, Z. Y. Li, M. Rycenga and Y. Xia, *J. Am. Chem. Soc.*, 2010, **132**, 2506-2507.

3 W. Zhang, J. Yang and X. Lu, *ACS Nano*, 2012, **8**, 7397-7405.

4 H. Guo, Y. Chen, H. Ping, J. Jin and D. L. Peng, *Nanoscale*, 2013, **5**, 2394-2402.

5 M. B. Cortie and A. M. McDonagh, *Chem. Rev.*, 2011, **111**, 3713-3735.

6 J. Huang, S. Vongehr, S. Tang, H. Lu and X. Meng, *J. Phys. Chem. C*, 2010, **114**, 15005-15010.

7 B. Liu, G. Han, Z. Zhang, R. Liu, C. Jiang, S. Wang and M. Y. Han, *Anal. Chem.*, 2012, **84**, 255-261.

8 Y. Ma, W. Li, E. C. Cho, Z. Li, T. Yu, J. Zeng, Z. Xie and Y. Xia, *ACS Nano,* 2010, **4**, 6725-6734.

9 M. Tsuji, K. Ikedo, M. Matsunaga and K. Uto, *CrystEngComm*, 2012, **14**, 3411-3423.

10 Y. Choi, S. Hong, L. Liu, S. K. Kim and S. Park, *Langmuir*, 2012, **28**, 6670-6676.

11 A. Muzikansky, P. Nanikashvili, J. Grinblat and D. Zitoun, *J. Phys. Chem. C*, 2013, **117**, 3093-3100.

12 H. Wang, Z. Sun, Y. Yang and D. Su, *Nanoscale,* 2013, **5**, 139-142.

13 N. Zhang, X. Fu and Y. Xu, *J. Mater. Chem.*, 2011, **21**, 8152-8158

14 L. Zhang and H. Wang, *J. Phys. Chem. C*, 2011, **115**, 18479-18485.

15 W. He, X. Wu, J. Liu, X. Hu, K. Zhang, S. Hou, W. Zhou and S. Xie, *Chem. Mater.*, 2010, **22**, 2988-2994.

16 H. Guo, Y. Chen, H. Ping, J. Jin and D. L. Peng, *Nanoscale*, 2013, **5**, 2394-2402.

17 S. Choi, Y. Hong and Y. Kang, *Nanoscale*, 2013, **5**, 7867-7871.

18 Y. Ye, L. Kuai and B. Geng, *J. Mater. Chem.*, 2012, **22**, 19132-19138.

19 R. Liu, F. Qu, Y. Guo, N. Yao and R. Priestley, *Chem. Commun.*, 2014, **50**, 478-480.

20 Y. Kim, J. W. Hong, Y. W. Lee, M. Kim, D. Kim, W. S. Yun and S. W. Han, *Angew. Chem. Int. Ed.*, 2010, **49**, 10197-10201.

21 Y. Lu and W. Chen, *ACS Catal.*, 2012, **2**, 84-90.

22 W. Wang, Y. Gao, X. Jia and K. Xi, *J. Colloid Interface Sci.*, 2013, **396**, 23-28.

23 H. You, S. Yang, B. Dinga and H. Yang, *Chem. Soc. Rev.*, 2013, **42**, 2880-2904.

24 F. Yu, W. Zhou, R. M. Bellabarba and R. P. Tooze, *Nanoscale*, 2014, **6**, 1093-1098.

25 X. Cao, N. Wang, S. Jia, and Y. Shao, *Anal. Chem.*, 2013, **85**, 5040-5046.

26 L. Y. Chen, T. Fujita, Y. Ding and M. W. Chen, *Adv. Funct. Mater.*, 2010, **20**, 2279-2285.

27 A. X. Yin, X. Q. Min, W. Zhu, W. Liu, Y.-W. Zhang and C. H. Yan, *Chem. Eur. J.*, 2012, **18**, 777-782.

28 B. Y. Xia, H. B. Wu, X. Wang and X. W. D. Lou, *J. Am. Chem. Soc.*, 2012, **134**, 13934-13937.

29 F. Nosheen, Z. C. Zhang, J. Zhuang and X. Wang, *Nanoscale*, 2013, **5**, 3660-3663.

30 C. Xu, Y. Liu, F. Su, A. Liu and H. Qiu, *Biosens. Bioelectron.,* 2011, **27**, 160-166.

31 M. Jin, H. Zhang, J. Wang, X. Zhong, N. Lu, Z. Li, Z. Xie, M. J. Kim and Y. Xia, *ACS Nano,* 2012, **6**, 2566-2573

32 M. Tsuji, X. Tang, M. Matsunaga, Y. Maeda, and M. Watanabe, *Cryst. Growth Des.*, 2010, **10**, 5238-5243.

33 A. Kumar, A. Saxena, A. De, R. Shankara and S. Mozumdar, *RSC Adv.*, 2013, **3**, 5015-5021.

34 M.Tsuji, M. Matsunaga, T. Ishizaki and T.Nonaka, *CrystEngComm*, 2012, **14**, 3623-3632.

35 B. Wiley, Y. Sun, B. Mayers and Y.Xia, *Chem. Eur. J.* 2005, **11**, 454-463.

36 M. Tsuji, M. Ogino, R. Matsuo, H. Kumagae, S. Hikino, T. Kim and S. H. Yoon, *Cryst. Growth Des.*, 2010, **10**, 296-301.

37 I. Pastoriza-Santos and L. M. Liz-Marza´n, *Adv. Funct. Mater.*, 2009, **19**, 679-688.

38 X. Xia, Y. Wang, A. Ruditskiy and Y. Xia, *Adv. Mater.* 2013, **25**, 6313-6333

39 Z. Guo, M. L. Seol, M. S. Kim, J. H. Ahn, Y. K. Choi, J.-H. Liu and X. J. Huang, *Nanoscale* 2012, **4**, 7524-7535.

40 X. Xia, S. Xie, M. Liu, H. C. Peng, N. Lu, J. Wang, M. J. Kim and Y. Xia, *PNAS*, 2013, **110**,

6669-6673.

41 J. Maroliand T. Kuwana, *Electrochimim Acra*, 1992, 37, 1187-l 197.

42. M. Jia, T. Wang, F. Liang and J. Hu, *Electroanalysis* 2012, **24**, 1864-1868.

43. L. Wang, X. Gao, L. Jin, Q. Wu, Z. Chen and X. Lin, *Sens. Actuators B,*2013, **176**, 9-14.

44. B. Fang, A. Gu, G. Wang, W. Wang, Y. Feng, C. Zhang, and X. Zhang, *ACS Appl. Mater. Interfaces,* 2009, **1**, 2829-2834.

45. Y. Zhao, J. Zhao, D. Ma, Y. Li , X.Hao, L. Li, C. Yua, L. Zhang, Y. Lu and Z. Wang, *Colloid Surf. A-Physicochem. Eng. Asp.*, 2012, **409**, 105-111.

46. X. Chen, H. Pan, H. Liu and M. Du, *Electrochim. Acta*, 2010, **56**, 636-643.

47. R. Ding, J. Liu, J. Jiang, J. H. Zhu and X. Huang, *Anal. Methods,* 2012, **4**, 4003-4008.